The Evolution of Crystalline Structure during Gel Spinning of Ultra-High Molecular Weight Polyethylene Fibers

The Evolution of Crystalline Structure during Gel Spinning of Ultra-High Molecular Weight Polyethylene Fibers[†]

Christopher K. Henry,[a] Giuseppe R. Palmese,[a] and Nicolas J. Alvarez[a]

Ultra-high molecular weight polyethylene (UHMWPE) fibers have been the subject of many investigations. Most studies are focused on the final mechanical properties of the fiber and the processing window required to achieve high modulus and tensile strength. Several studies have alluded that the crystalline morphology developed during gel spinning and post drawing are very important in final mechanical properties. However, it is surprising to know that no clear correlation exists between crystalline structure and initial, evolving, and final mechanical properties. In an attempt to define structure-property relationships, we have developed novel tools to quantify the effect of processing on crystalline structure evolution. We examine through controlled gel-spinning and SAXS analysis the effect of flow kinematics on the development of crystalline structure. Direct correlations are made between polymer solution relaxation time, extension rates, crystallization time and gel-spun crystalline morphology. We report direct evidence of flow induced crystallization, which approaches an asymptotic crystallization rate at high Weissenberg number. For Wi<1, the crystalline structure is only slightly affected from equilibrium. For Wi>1, the crystalline structure is highly anisotropic due to chain orientation/stretch during spinning. Fibers spun at different Weissenberg numbers are drawn to low draw ratios at constant temperature to measure the initial structure evolution. A qualitative SAXS analysis clearly shows similar evolution of different starting structures with formation of more straight chain crystals upon drawing. However, there remains quantitative differences between the length of straight chain crystal and the size and distribution of lamellae domains depending on the starting structure.

1 Introduction

Ultra-high molecular weight polyethylene (UHMWPE) fibers are of considerable interest for their use in extreme dynamic environments[1]. The most successful process of producing strong UHMWPE fibers uses two sequential operations: gel spinning followed by post drawing[2,3]. In the gel spinning process, a dilute polymer solution is extruded from a nozzle and solvent is subsequently removed either by evaporation or solvent extraction. The as-spun crystalline fiber (ASF) is then passed into the drawing stage whereby the temperature is controlled below melting and a tensile stress is applied. The fiber diameter is decreased via tensile loading to a desired draw ratio. The fiber after this stage is denoted as the post drawn fiber (PDF). While prior studies have focused on producing fibers with remarkable tensile modulus, tenacity, and strength from the gel spinning process[2,4–10], very few studies investigate the importance of structure evolution

during processing that gives rise to such properties. In the early developments, characterization was primarily limited to drawn fiber microstuctures through wide angle x-ray scattering (WAXS) to determine crystalline orientation and deformation[2,6,10] and polarization/electron (SEM and TEM) microscopy imaging[5,6,8] to show qualitative macrostructures.

In the literature, more emphasis has been placed on the importance of processing parameters such as gel concentration, solvent quality, molecular weight distribution, velocity ratios, temperatures, and maximum draw ratio (DR) on final PDF performance[2,5–7,11–16]. The culmination of these studies have outlined that low concentration (1-5 wt%)[15], high molecular weight, low polydispersity[16], low ASF draw ratio[17], and a temperature gradient during drawing lead to the highest performing fibers[18].

From the initial work in the area of solution cast UHMWPE, there is considerable evidence that straight chain crystals (shish), first shown by Pennings[19,20], are necessary for PE to achieve high tensile properties[21–23]. In the extended state the covalent bonds of the carbon backbone bear the applied load, as opposed to the comparatively weak Van der Walls forces of a random coil system[24]. The tendency to form straight chain crystal within a fiber is strongly dependent on the so-called "drawability" of the

sample, which is argued to depend on (1) the existence of an α-relaxation time[21,25], (2) the number of entanglements[23,26], and (3) the starting as-spun structure morphology[16,27]. Requirement (1) is solely dependent on the chemical repeat unit of the polymer. Requirement (2) and (3) are dependent on processing conditions and history. Hoogsteen and coworkers argue that little to no draw should be applied during the gel spinning process to avoid the formation of defects denoted as "tight knots" and cold drawing that results in chain scission[17,27]. The authors argue that ASF consisting of isotropic lamellae crystalline domains exhibit the highest degree of "drawability". This point was recently brought into question by Ohta and coworkers who demonstrated that drawing during spinning does not necessarily influence the "drawability" of the fibers. In fact, highly drawn fibers during spinning resulted in equally strong tensile fibers after post drawing[28].

The state of the art leaves several questions unanswered: (i) What processing parameters control the initial crystalline structure? (ii) What is the role of flow induced crystallization in determining the as-spun fiber structure? (iii) To what extent does the initial as spun crystalline structure determine the final drawn crystalline structure?

One difficulty in answering these questions is that previous work has not characterized gel spinning parameters in quantitative terms. Typically, processing parameters are presented in relative terms, e.g. velocity ratios, absolute spinline velocities, and extrusion rate[9,23]. Relative parameters do not allow for a direct correlation between process and structure, since their value are specific to a given experimental setup. Answers to the above questions require detailed quantification of the effect of flow during spinning on the state of the polymer chain in solution. De Gennes originally hypothesized that a polymer chain in dilute solution undergoes an abrupt transition from a random coil state to an extended chain configuration under extensional flow[29]. From the kinetic theory of polymers it can be shown that this transition is expected when the extension rate is $1/2$ the inverse relaxation time of the polymer chain, i.e. when the Weissenberg number, Wi$= \tau_d \dot{\varepsilon}_d \geq 0.5$, where $\dot{\varepsilon}_d$ is the strain-rate applied during spinning and τ_d is the characteristic disengagement time measured from linear viscoelasticity. This transition was captured by the single DNA measurements of Chu and coworkers, whereby the DNA chain went from random coil to a saturated stretched length in a reasonably short experimental time[30]. While single molecule dynamics are nontrivial in gel-spinning, understanding the kinematics of the flow field will allow for quantitative comparison of processing history and final molecular structure.

To answer (i)-(iii), we have developed a spinning and drawing apparatus that controls and measures the kinematics of the extensional flow imposed on the gel and fiber, respectively. These new tools allow for the measurement of strain, strain-rate, and crystallization rate as a function of time, leading to a full quantitative description of the processing history. Fibers are then analyzed via small angle x-ray scattering to quantify the effect of processing history on crystalline structure. Orientation of the crystalline structure is quantified via Hermans' orientation factor, while the length and size of the lamellae and straight chain crystals are analyzed via Bragg peak analysis and Ruland streak analysis, respectively. We investigate the influence of maximum and average Wi during spinning on the final ASF crystalline structure. We show that there is a direct correlation between maximum Wi and the as-spun crystalline morphology, e.g. increasing Wi moves the crystalline morphology from isotropic lamellae to axially oriented lamellae to lamellae oriented perpendicular to flow. For Wi<1.5 there is a correlation between increasing Wi and decreasing crystallization time (i.e. flow induced crystallization). However for Wi>1.5 the crystallization time is relatively constant, but the crystalline morphology is still progressing towards extended chain crystals. Percent crystallinity follows a similar trend as observed from WAXS data. Finally, we show that there is a direct relationship between the ASF crystalline structure and its evolution during drawing for low draw ratios.

2 Experimental Methods

Solution Preparation: 8wt% polymer solutions are made from a mixture of UHMWPE ,3-6M Mw (Sigma Aldrich CAS9002-88-4, Batch), and Decahydronaphthalene (Decalin) (Sigma Aldrich CAS911-17-8). Both chemicals are used as received. Gel permeation chromatography (GPC) is performed on the UHMWPE powder to verify the molecular weight distribution; see supplementary information for details. The dilute gel solutions are loaded into 30 cm^3 stainless steel cylinders and placed into a hybridization oven at 150°C, where the samples are rotated at 20rpm for 16hrs around the central axis of the oven. This preparation method is used in place of mechanical mixing to prevent reduction in molecular weight. The resulting sample is a highly elastic clear polymer solution. This gel is extruded directly from the cylinder at 150°C into the gel-spinning apparatus.

Gel Characterization: Small amplitude oscillitory shear (SAOS) experiments are performed to determine the relaxation behavior of the dilute polymer solutions. The 8wt% gels are tested on a Discovery Hybrid Rheometer 3 (TA Instruments), using 8mm parallel plate with electronically heated plates for temperature control. The DHR3 is preheated to 120°C to prevent crystallization prior to the testing. A solvent trap is arranged around the plates to prevent evaporation of decalin. The strain amplitude is 1% which is in the linearvicoelastic regime as determined from an amplitude sweep. The relaxation behavior is determined by a frequency sweep spanning five decades.

A Q2000 (TA Instruments) Differential Scanning Calorimeter (DSC) is used to measure crystallization temperature, and isothermal crystallization kinetics. A 10-20mg sample of premixed gel solution is loaded into hermetically sealable T Zero aluminum DSC pans. To ensure complete removal of all prior thermal history the gel is held at 150°C for 10min prior to cycling. The highest temperature at which crystallization occurs is $T_c = 81°$, and is found by cycling the gel between 50-120°C at 1°C/min. Isothermal crystallization kinetics are measured following guidelines reported by Lorenzo and coworkers[31]. Samples are held at 150°C for 10min to clear thermal history, and then equilibrated at 120°C before ramping at 40°C/min to T_c. Samples are held isothermally at T_c for 30min to observe crystallization. Heat flow versus time is fit to the Avrami equation; $1 - V_c = exp(-kt^n)$.

In the Avrami, V_c is the volume fraction of crystalline material, n is the Avrami index, and k is the crystallization rate constant. The half crystallization time, i.e. the time to reach 50% volume percent of crystals at the crystallization temperature T_c, obtained from this fit is $t_{1/2} = 53$s. $t_{1/2}$ represents the time for crystallization of an isotropic, isothermal extrudate held at 81°C. Note that during spinning the material is neither isotropic nor isothermal. Given that the sample leaves the nozzle at 120°C and must cool a $\Delta T = 39$°C to begin crystallization, $t_{1/2}$ represents a conservative lower bound on the isotropic crystallization time. Thus we will use the definition of $\tau_k < t_{(1/2)}$ to signify flow-induced crystallization.

Gel Spinning Apparatus: The solution is gel-spun in a novel apparatus detailed in Figure 1. The apparatus provides precise control of temperature, flow rate, take up velocity, and various quenching parameters. A constant gel flowrate, Q, is controlled via a piston mounted to a feedback closed loop linear slide motor (Oriental Motors, EASM4RXE050ARMC) with an adjustable velocity (minimum velocity=0.001 mm/s), V_{piston}. The stainless steel hopper is temperature controlled via a band heater and was held at a constant T_{hopper}=120 °C for all experiments reported. The gel is extruded at a velocity, $V_{nozzle} = f(Q, D_0)$, which is a function of the set flowrate Q and the nozzle diameter D_0, from a nylon type heated nozzle held at a constant T_{hopper} =120 °C, (Plastics Processing Equipment, RTEG334118) into a convection oven passing countercurrent dry air at room temperature. The oven is equipped with optically transparent sides such that a laser micrometer (Keyence, LS-7501), mounted on an additional linear slide motor, is positioned to measure the gel (extrudate) diameter as a function of position from the nozzle tip. The micrometer is equipped with a camera that views the fiber in transmission mode. A system of rollers and motors are positioned to handle and collect the fiber after exiting the oven. There are numerous ways to configure the rollers and motors. Two configurations are utilized in this work and are shown in Figure 1: Setup 1 consists of a constant velocity motor with velocity $V_{wind-up}$ to takeup the fiber as it is extruded and Setup 2 consists of the constant velocity motor for spinning followed by a constant torque motor to maintain tension on the fiber. Note that Setup 2 is more common in practice as it maintains a constant $V_{wind-up}$, whereas Setup 1 $V_{wind-up}$ is increasing with the amount of fiber wound on the roller. After spinning, the fibers are unspooled and the excess decalin is evaporated in a vacuum oven overnight at 50°C. Care is taken not to cold draw or apply any stress to the fiber before the drawing stage. Note that inadvertent cold drawing would be observed via crazing along the fiber length. Dried fibers are denoted as As Spun Fibers (ASF) and are ready for post-drawing. Results obtained using Setup 1 are reported using square symbols in all figures, conversly Setup 2 results are triangle symbols. Two V_{nozzle} magnitudes are used; fibers spun with V_{nozzle}=1.25 mm/s are represented in blue, fibers with V_{nozzle}=2.5 mm/s are red.

As Spun Fiber Characterization: Typically, the gel spinning process is characterized by a velocity ratio, VR= $V_{wind-up}/V_{nozzle}$, however the micrometer allows for a detailed analysis of the flow kinematics near the nozzle tip. Figure 2 first shows the profiles of three different fibers at different VRs as a function of distance
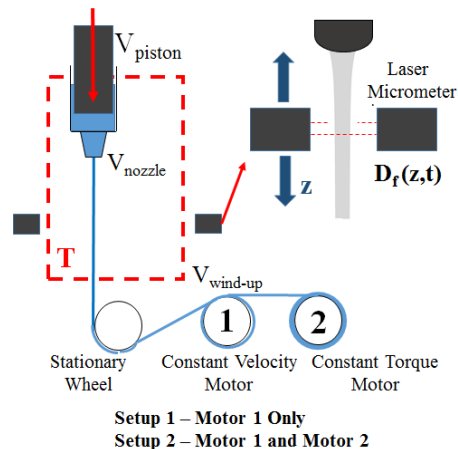

Fig. 1 Cartoon of the gel-spinning apparatus. A laser micrometer is mounted to a motor around the oven. Downstream fiber handling has 2 Setup's: (1) a constant velocity motor provides draw to the system and spools fiber (2) A constant torque wind-up motor is positioned after velocity motor and spools the As-Spun fiber.

from the tip of the extrusion nozzle. The fiber profiles begin at the nozzle tip and continue until a final distance, which is the observed crystallization point.

During spinning, crystallites are observed to form in the center axis of the fiber via the in-situ optical camera. The crystallization point is defined as the distance from the nozzle where light is no longer transmitted through the center axis of the fiber. While the micrometer measures diameter as a function of position, $D(p)$, using conservation of mass and a constant volumetric flowrate, the velocity at each position can be calculated. Knowing $D(p)$ and velocity allows for the determination of diameter as a function of time, $D(t)$, as shown Figure 2 (b). The point of crystallization is reported in units of time and denoted τ_k. Figure 2 alludes to the development of flow induced crystallization since τ_k depends on the flow kinematics. Note, the estimated evaporative flux of decalin from a planar surface was measured using Thermal Gravimetric Analysis (TGA) to be $J_{evap} = 3.62$ g/m^2/s. Decalin is pipetted into a crucible of known dimensions and then ramped at 40°C/min to 120 °C and held for 10 min under inert atmosphere to measure mass lost through evaporation. This translates to a conservative estimate of diameter decrease due to evaporation of 200μm over 50s. Therefore solvent evaporation is assumed negligible in fiber diameter measurements up to the crystallization point.

The true Hencky strain is calculated from, $\varepsilon_d(t) = 2\ln(\frac{D_0}{D(t)})$, where $D(t)$ is the diameter at any given time t.[32] Figure 3 (a) shows strain as a function of time for the three profiles reported in Figure 2. All three VRs show a fast increase in Hencky strain near the nozzle (early time), followed by a slow increase in Hencky strain at approximately $t > 5$ s. Note that not all measurements start at a $\varepsilon_d = 0$ as fiber pullout occurs at high velocity ratios[33]. The slope of strain versus time leads to the instantaneous applied strain rate and is shown in Figure 3 (b), the inset focuses on the instantaneous strain rate at short times. For all three profiles, 3 (b) shows an initial high strain-rate near the nozzle that quickly
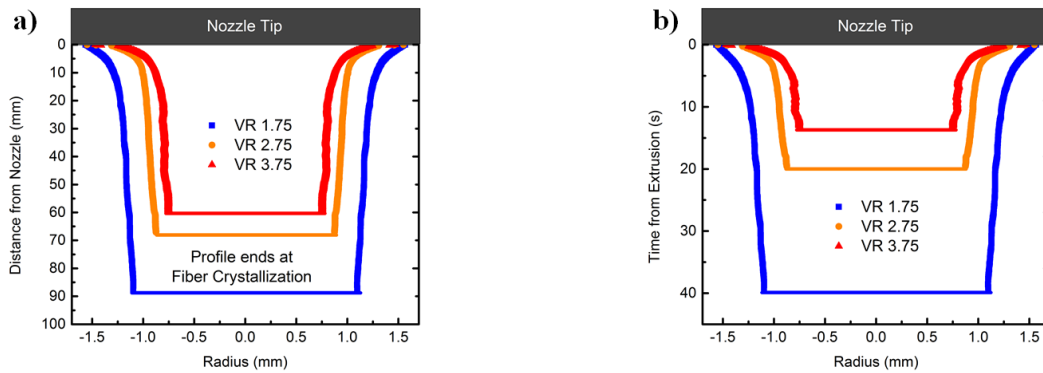
Fig. 2 Fiber profiles of 3 fibers spun at different VR plotted as functions of (a) distance from the nozzle (b) time from the nozzle.

decays to zero as the fiber approaches the crystallization point. This data clearly shows that a higher VR leads to a higher maximum initial strain-rate, $\dot{\epsilon}_{d\,\max}$. The average strain rate applied, $\dot{\epsilon}_{d\,\mathrm{avg}}$, is calculated from the maximum strain divided by τ_k.

Drawing Apparatus: For accurate and controlled drawing of the samples an extensional rheometer, VADER 1000 (Rheo Filament ApS), was modified for use as a drawing apparatus. Capstan style clamps, shown in Figure 4, were designed to hold the fibers during drawing. The fiber is held in place by the planar clamp and wrapped around the circular capstan to delocalize stress along the clamp edge. A convection oven controls temperature to $T_{\mathrm{draw}} = 120°C \pm 0.1 °C$ for all experiments reported. A laser micrometer monitors the deformation of the fiber at a set position, typically the center distance between capstans. While the VADER 1000 allows for drawing at constant stress, strain-rate, or velocity, all measurements were carried out at constant velocity, $V_{\mathrm{draw}} = 0.5$ mm/s, to simulate the drawing between rollers on an industrial fiber line. The draw ratio is reported in terms of the measured decrease in diameter, $\mathrm{DR}_D = (D_{0,\mathrm{ASF}}/D(t))$. The gage length before drawing is held constant at $L_g = 30$ mm for all samples. The amount of strain in diameter is not uniform over the gage length. We observed local formation of necks that subsequently propagated with increasing DR_L Samples can be drawn to a maximum of $\mathrm{DR}_L = 4$, i.e. $\mathrm{DR}_D = 2$ in a single draw. For samples with $\mathrm{DR}_D > 2$, a uniform segment from the first draw is reloaded to allow for further draws.

Crystalline Morphology Characterization: Small and Wide Angle X-ray Scattering (SAXS and WAXS) measurements were performed using a Rigaku SMAX-3000 with a MicroMax-002 sealed tube x-ray source operated at 45kV and 0.88mA. Cu-KÎś radiation is generated with a wavelength of 0.154nm. A gas filled proportional type detector that is 200 mm in diameter with a 20 μm resolution collects the scattering signal. The SMAX-3000 environment is 3 meters long and is fully evacuated prior to sample exposure. The beam focal spot is 20μm x 20μm. Samples are placed on a plate mounted to a X-Y scanning motor allowing for precise 2D sample positioning. The plate is composed of grooved channels that align the fiber axis horizontally with respect to gravity. The center of the sample is determined by minimizing transmitted intensity measured at the beamstop. Measured scattering vectors($q = \frac{4\pi}{\lambda} sin\theta$) range from 0.0067 to 0.16

A^{-1}. Typical exposure times are 15 minutes for the samples presented here. To perform wide-angle analysis an image plate must be manually inserted and adjusted to sit 30mm to 200mm from the sample. This provides a second range of measureable scattering vectors that range from 0.11 to 4.9 A^{-1}. Silver behenate and silicon powder are used to calibrate for the small-angle and wide-angle measurements respectively. To measure percent crystallinity, single fiber WAXS patterns are deconvoluted and peak areas are summed and compared, and further details are presented in the supplementary data. All 2D patterns are analyzed with both Datasqueeze (Paul Heiney, www.datasqueezesoftware.com) and the Rigaku SAXS GUI software package provided with the instrument.

3   Results and Discussion

3.1   Gel Spinning

Effect of Strain Rate on τ_k: The gel spinning apparatus affords the measure of the crystallization time, τ_k, as described in the methods section. Figure 5 shows average τ_k values as a function of VR for a wide range of experiments. The uncertainty is the standard deviation which is based on six measurements taken over the duration of the spinning process. Duplicate experiments of VR=2.4 and VR=3.3 were performed to ensure reproducibility. The different colors represent unique configurations of the spinning apparatus as detailed in the caption and methods section. Regardless of setup, there is an inverse proportionality between τ_k and VR, but different setups have different magnitudes of τ_k.

Table 1 compares the processing parameters for three experiments (Cases) at VR=1.75. Case 1 and Case 2 correspond to experiments using setup 1 and setup 2 at the same V_{nozzle} respectively. The change in setup leads to a 16% decrease in τ_k. The difference in τ_k between setups is magnified at higher velocity ratios. This result implies that each experimental setup will have a unique dependence of τ_k on VR. The difference between Case 2 and Case 3 is the magnitude of V_{nozzle}. Although at the same VR, Case 3 shows a 28% decrease in τ_k compared to Case 2. This clearly shows that VR does not capture the relevant physics to describe the mechanism of structure formation in the spinning process. Futhermore, the strong dependence of τ_k on processing parameters suggests flow induced crystallization, FIC. FIC is known to arise in the presence of strong shear and extensional
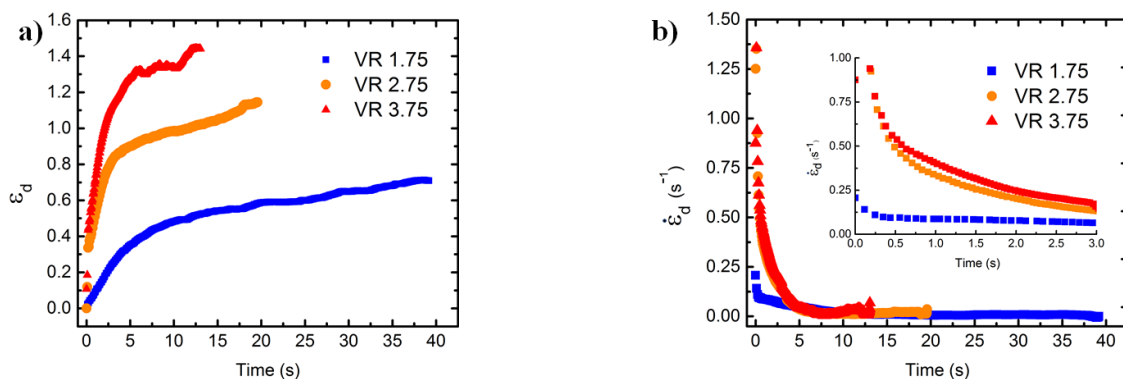
Fig. 3 (a) The strain as a function of time from exiting the nozzle for three different VR cases. (b) Strain Rate as function of time. Inset shows the cases during the first three seconds of the spinning process.

Fig. 4 Clamps developed to hold the spun UHMWPE fibers during post drawing.
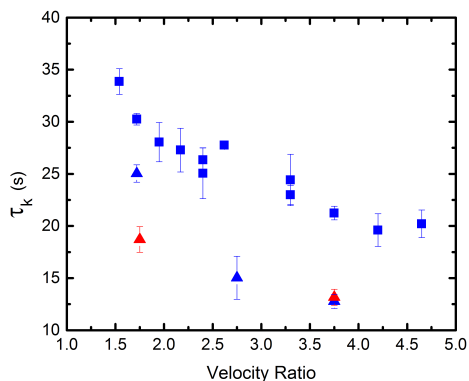

Fig. 5 Crystallization time, τ_k, as a function of velocity ratios for different experimental setups. Square symbols represent Setup 1. Triangles correspond to Setup 2. Color represents V_{nozzle}. Blue represents fibers spun at V_{nozzle}=1.25mm/s. Red were spun at V_{nozzle}=2.5mm/s

flows[34–41]. Note, that FIC is defined when $\tau_k \leq t_{1/2} + t_{81}$, where t_{81} is the time required for the extrudate to reach T_c. We conservatively estimate t_{81}=20s from Figure 5.3-8 in Geankoplis by assuming a constant diameter cylinder of D=1.3mm (ε_d =1.75), a convective heat transfer coefficient, h=25 W/m^2/K, and a thermal diffusivity of decalin $\alpha = 7.62 \times 10^{-8}$ m^2/s[42]. Note that for all experiments $\tau_k < t_{1/2} + t_{81} \approx 73$ s, which indicates significant FIC even for the lowest VRs.

It is well known that the crystallization time is strongly dependent on the relative orientation of the polymer chains, as seen in shear flow experiments[36,38,40,43]. Extensional flow is much more effective at stretching chains than shear and therefore expected to have a stronger effect on the crystallization time. In polymer physics the degree of chain orientation and stretch is quantified by the Weissenberg number, which is a ratio of the chain relaxation time to the time scale of the flow (inverse strain rate). In a typical gel-spinning experiment the strain rate is a function of distance from the nozzle, ie. time, see methods section. It is unclear whether $\dot{\varepsilon}_{max}$ or $\dot{\varepsilon}_{avg}$ is the relevant inverse time scale to capture the observed physics. If we reexamine the three cases in Table 1, we observe that Case 1 and Case 2 have the same $\dot{\varepsilon}_{avg}$ but different $\dot{\varepsilon}_{max}$. Thus $\dot{\varepsilon}_{max}$ appears more relevant in explaining differences in τ_k, Figure 6a shows all τ_k as a function of $\dot{\varepsilon}_{max}$. Unlike Figure 5 we see a single master curve independent of experimental setup and absolute velocity. Given $\dot{\varepsilon}_{max}$ the application of Wi number is only missing a characteristic relaxation time of the polymer, τ_p.

Typically, τ_p is taken to be the Rouse time, $\tau_R = \tau_c Z^2$, where τ_c is the relaxation time of one entanglement and Z is the number of entanglements per chain. Unfortunately, the Rouse time is not easily defined for semicrystalline polymers since the measure of τ_c is nontrivial due to $T_m >> T_g$. In some cases τ_d, the longest relaxation time, is used in place of τ_R, since they are proportional to each other, and τ_d is relatively easy to measure via SAOS data[44,45]. The inset in Figure 6b shows a frequency sweep of elastic, G', and viscous, G", moduli measured in SAOS for an 8wt% UHMWPE gel at 120°C. We denote the characteristic relaxation time to be $\tau_d = 1/\omega_d$=6.7 s, where ω_d is the highest frequency in Figure 6b where G'=G". Note that for a monodisperse entangled linear polymer gel, this timescale would be equivalent

Table 1 Gel Spinning data for three samples spun at a constant Velocity Ratio

Sample Run	VR	V_{nozzle} (mm/s)	V_{windup} (mm/s)	TorqueMotor [Y/N]	τ_k (s)	$\dot{\varepsilon}_{d\,\text{max}}$ (1/s)	$\dot{\varepsilon}_{d\,\text{avg}}$ (1/s)
Case 1	1.75	1.25	2.2	N	30	0.10	0.03
Case 2	1.75	1.25	2.2	Y	25	0.12	0.03
Case 3	1.75	2.5	4.4	Y	18	0.19	0.04
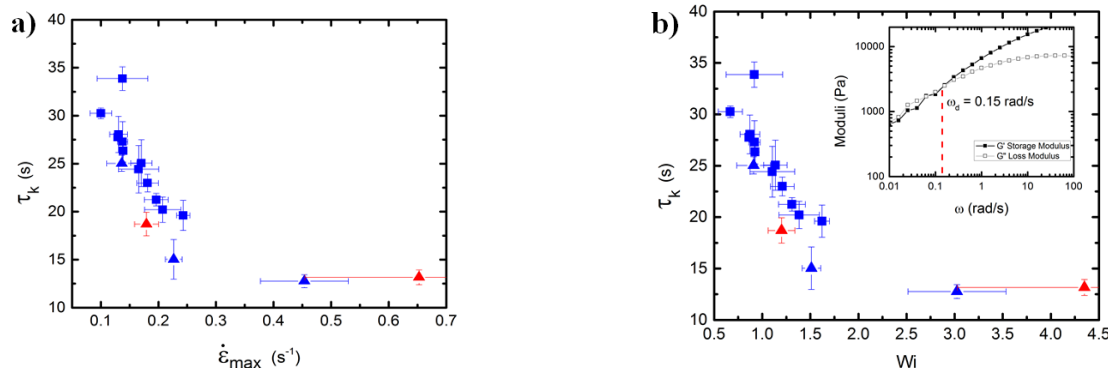
Fig. 6 τ_k as a function of (a) max strain rate, $\dot{\varepsilon}_{max}$ and (b) Wi.

to the disengagement time. However, due to the broad distribution of Mw present in UHMWPE samples, a terminal relaxation is not observed. Thus the chosen τ_d is in fact the lower bound of a distribution of longest relaxation times.

Figure 6b shows all values of τ_k plotted as a function of Wi, with $\tau_p = \tau_d$. Note that unlike Figure 5, there is a clear master curve indicating that Wi captures the relevant physics of the spinning process. The data shows that the largest decrease in τ_k occurs at low Wi, while high Wi appears to have a limiting value of τ_k. In uniaxial extension, Wi<0.5 translates to orientation of the chain with very little stretching, while Wi>0.5 is indicative of stretching of the chain, when Wi is defined in terms of τ_R [46]. Our data implies significant FIC for increasing orientation and only a slight increase for significant chain stretching. Note that the reported Wi is in terms of τ_d and thus would be much smaller in magnitude when defined in terms of τ_R due to $\tau_d > \tau_R$. While the decrease of τ_k with increasing Wi is expected the observed asypmtotic behavior at high Wi has two possible explanations: (1) there is an asymptotic limit to the flow enduced reduction of the entropic barrier for crystallization, or (2) the absolute strains during spinning are not large enough to strongly affect orientation and stretching. It is well documented that $\varepsilon_d >1$ is necessary to see departure from the linear viscoelastic response of the polymer melt/solution, and observe a Wi effect on chain orientation and stretch [45,47]. Figure 7 shows the measured Hencky strain at the crystallization point, $\varepsilon_{max,d}$, for the experiments presented previously. All Wi>1.5 experiments show $\varepsilon_{max,d} >1$ which signifies increasing Wi can cause higher degrees of chain orientation and stretch, and as such it is unlikely that explanation (2) is causing the asymptotic behavior. Furthermore the work of Rutledge and coworkers strongly supports explanation (1). Nicholson et. al. used Molecular Dynamics simulations of monodisperse n-eicosane melts to quantify the effects of extensional flow fields on crystallization kinetics.[48] They conclude flow-enhanced nu-
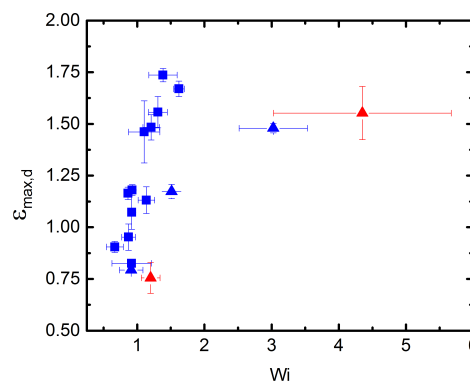
Fig. 7 Hencky strain, $\varepsilon_{max,d}$, at the crystallization point as a function of Wi, as measured during gel-spinning.

cleation behavior is dominated by a critical strain rate. When the ratio of the applied strain rate to the critical rate is less than one, Wi<0.06, nucleation kinetics are effectively those of quiescent nucleation. Above unity, Wi>0.06, nucleation is sped up due to chain alignment reducing the entropic barrier. For ratios greater than five, Wi>1, the energetic barrier reaches an asymptotic minimum. Incidentally, the crystallization rate continues to increase with Wi due to "diffusive" contributions occurring in the melt. However, in the case of a dilute polymer solution, diffusive contributions are not expected to contribute strongly to an increase in kinetic rate due to large distances between stretched chains. Therefore the asymptotic limit of τ_k with increasing Wi observed here can be argued to coincide with explanation (1): an asymptotic limit of the energetic barrier. Note that this implies that the crystallization rate in a given kinematic flow field will strongly depend on the concentration of polymer: up to the neat melt.

Before we examine the effects of drawing, we would like to address the impracticality of utilizing Wi to control a true commer-
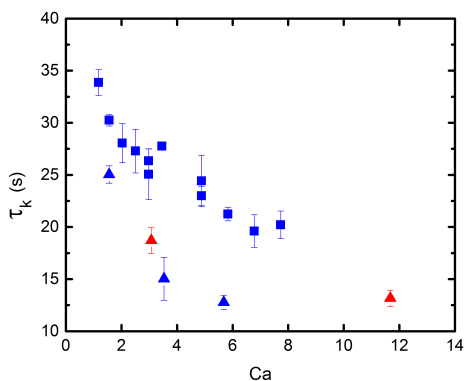
Fig. 8 τ_k as a function of Ca of the gel spun fibers.

cial process. The measure of $\dot{\varepsilon}_{max}$ is impractical in a commercial spinning process due to nonconstant flow rate, the use of multiple nozzles in a single spinneret, and difficult working conditions. A potential alternative dimensionless group that characterizes the deformation in a two-fluid system is the Capillary number (Ca).

The Capillary number has been used in creeping flow experiments to determine the effect of extensional stress on interface deformation, and is a ratio of viscous forces to restoring surface tension forces, given by,

$$Ca = \frac{\dot{\gamma}\mu L_c}{\sigma} = \frac{\mu(V_{wind-up} - V_{nozzle})}{\sigma}, \qquad (1)$$

where the characteristic strain-rate, $\dot{\gamma}$, times the characteristic length scale, L_c, is approximated as the difference in $V_{wind-up} - V_{nozzle}$.[49,50] The dynamic viscosity, μ, and surface tension, σ, were approximated as 50 Pa·s and 0.03 Nm^{-1} respectively The Reynolds number for all experiments is order 10^{-4}. Note that in creeping flow studies, Ca>1 is significantly large, and results in large deformations of the interface[51,52]. The values of τ_k are replotted as a function of Ca in Figure 8. The fibers spun with a greater absolute velocity difference exhibit a shift that causes the observed τ_ks to begin to approximate a master curve for Setup 2. In other words, for a given configuration, the Ca is useful in correlating the relative strength of the flow as compared to restorative surface tension forces. While Ca does not result in a master curve of τ_k, it is useful in capturing the effect of changes in absolute velocities. We do not intend to imply that Ca number is the appropriate scaling of τ_k, our results clearly show that Wi is the appropriate scaling. We only intend to highlight that the scaling of τ_k with ΔV does seem to collapse the data of a given experimental setup; meaning that ΔV is some measure of the applied strain rate. This is useful since ΔV is a readily obtained parameter from any spinning setup, whereas the applied strain rate is not easily measured. Note that a scaled velocity of $\frac{\Delta V}{V}$ does not capture changes in τ_k as seen in Case 2 and Case 3 in Table 1. These two cases have the same $\frac{\Delta V}{V}$, but very different τ_k.

Effect of strain rate on Crystalline Morphology: We have indirectly shown, via Wi, a relationship between the crystallization rate and flow induced chain morphology. A more direct indicator of flow induced chain morphology is the crystalline structure. We expect that oriented chains should form oriented lamellae,

while stretched chain should form straight chain crystals. Figure 9 shows 2D SAXS patterns for increasing Wi. Note that for Wi=3 and 4 that exposure time was kept constant, and apparant increase in scattering intensity is due to beam maintanence in between data collection. The solution cast film's 2D SAXS pattern is representative of polydisperse isotropic lamellae crystalline domains. For Wi=0.67 and 0.86, where one would expect orientation of the chains within the spinning flow field, the 2D pattern indicates polydisperse lamellar crystals with slight preferential orientation in the fiber axis direction. The 2D SAXS pattern for Wi=1.3, where the chain should be undergoing some degree of stretch, indicates a tighter distribution of lamellae oriented in the fiber direction with the beginnings of straight chain crystal formation. For Wi>1.3, the 2D pattern shows the same propensity of straight chain crystal formation, but a drastic shift in the lamellae orientation: from oriented along the fiber axis to oriented perpendicular to the fiber axis. This suggests a flow induced transition to the well-characterized "shish-kebab" structure discussed in the literature. Interestingly, Wi=3 and 4.3 appear to have very similar 2D scatter patterns, in line with the asymptotic behavior of τ_k.

Hermans' orientation factor (f) is typically used to quantify the degree of alignment from 2D SAXS patterns and is given by,

$$f = \frac{3 < \cos^2 > -1}{2} \qquad (2)$$

$$< \cos^2 > = \frac{\int_0^{\frac{\pi}{2}} I(\phi)\sin(\phi)\cos(\phi)^2 d\phi}{\int_0^{\frac{\pi}{2}} I(\phi)\sin(\phi)d\phi}, \qquad (3)$$

where I is the measured relative intensity at a given scattering angle ϕ measured from a reference axis. We have chosen the convention of $\phi = 0$ along the fiber axis. Details of the Hermans' orientation quadrant and fitting algorithm are described in the supplementary text. The following limits are defined: $f = 0$ indicates no alignment of the crystalline domains, i.e. isotropic scattering, $f = 1$ indicates perfect alignment of crystals perpendicular to the fiber axis , while $f = -0.5$ indicates perfect alignment of crystals parallel to the fiber axis. Figure 10 (a) shows Hermans' orientation factor as a function of Wi for the 2D SAXS patterns shown in Figure 9. As expected, the solution cast sample (Wi= 0) shows $f \approx 0$ confirming the isotropic nature of the crystalline domains. f goes through a negative minimum for Wi< 1, indicating a maximum orientation in the fiber direction. For Wi≈2 the lamella shift from an orientation parallel to the fiber axis to one that is predominately perpendicular. At sufficiently high Wi, there is very little additional alignment of the lamellae crystalline domains.

Figure 10 (b) shows the measured percent crystallinity as a function of Wi, calculated using WAXS. See the supplementary data for details of the analysis. The solution cast sample is 74% crystalline, which is in agreement with various ASF and precursor samples reported in the literature[53–55]. The percent crystallinity increases approximately 5% for Wi< 1.3, where each of these fibers display similar crystallinities at around 79%. 80% crystallinity is the maximum observed, and as Wi is increased further a drop of 4% is observed in percent crystallinity. Note that per-
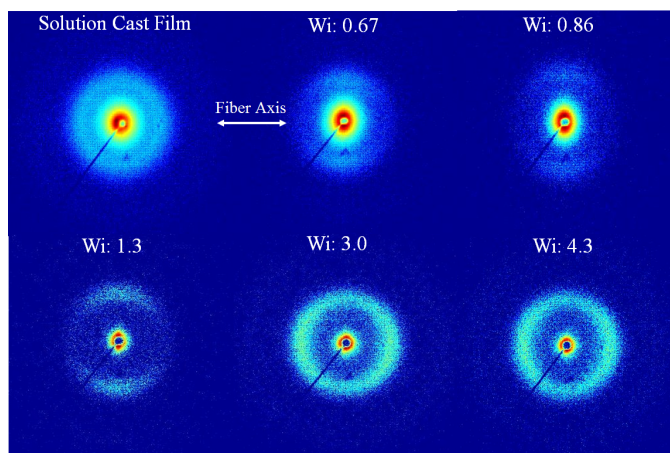
Fig. 9 2D SAXS patterns for ASF with different Wi number during gel spinning.

cent crystallinity does not show significant differences as Wi in increased during spinning from 3 to 4, i.e. an asymptotic value is reached. Suprisingly the observed asymptotic behavior of τ_k at high Wi is mirrored qualitatively in the 2D SAXS patterns, and quantitatively in Hermans' orientation factor and percent crystallinity .

3.2 Post Drawing

The ASFs are typically drawn on a large scale commercial setup that does not allow for characterization of the crystalline structure at early DR. Using the VADER 1000, small draw ratios are applied to the ASFs to quantify the evolution of the crystalline structure. Figure 11 shows four ASF drawing structures organized along the first column and the corresponding post drawn structures at a DR_d defined at the top of the column. For DR_d=1.7, there is a drastic shift in the scattering profile of the ASF. In all four cases, there is an immediate shift from a largely isotropic lamellar pattern to an anisotropic structure with distinct vertical streak features. The size and shape of the streak is indicative of the straight chain crystal dimensions. The Wi=0.67 ASF has qualitatively the longest straight chain crystal domains, which will be quantified later. It is more difficult to draw comparisons for the higher Wi fibers. In the higher Wi ASF a secondary structure to the left and right of the beamstop is highly visible and is indicative of perpindicularly oriented lamella. The lack of these patterns in low Wi ASF indicate a lower frequency of these domains or a domain size outside the available scattering vector window. Overall Figure 11 highlights the unique dependance of the drawn crystalline structure on the beginning ASF structure.

Using the Ruland Streak method we quantify the differences in straight chain crystal morphology as a funciton of DR_d for the four ASF cases.[56–58] Ruland showed that longitudinally oriented voids in between carbon fibers would generate a streak in the reciprocal scattering space. The azimuthal width of this streak, B_{obs}, can then be used to determine the average size, $\langle L_{shish} \rangle$, and the misorientation, B_ϕ, of the scattering element. The relationship used to fit the parameters is dependent on the function used to model B_{obs}. If B_{obs} is best fit with a Lorentzian curve then

the relationship is linear as shown in Eq. 4.

$$B_{obs} = \frac{1}{\langle L_{shish} \rangle s} + B_\phi \tag{4}$$

When B_{obs} is modeled using a Gaussian distribution then the relationship that is used is that shown in Eq. 5.

$$B_{obs}^2 = \left(\frac{1}{\langle L_{shish} \rangle s} \right)^2 + B_\phi \tag{5}$$

A detailed description of the Ruland streak method is outlined in the supplementary information.

Keum et. al. used this technique to study the formation of shish in shear flows from bi-disperse blends of PE[59]. They found that a Lorentzian model was a better fit for their data, and showed an ultimate average shish length of 900nm. The development of shish in our fibers is shown in Figure 12 where both the Gaussian and the Lorentzian equations are used respectively. The Gaussian function is better suited for the low DR_d samples that included significant azimuthal scattering near the beam stop, and the high DR_d samples are best modeled using the Lorentzian function. Both methods are reported to confirm the accuracy of the results. Regardless of the fit function the same trends in shish length are found. As DR_d increases the shish length shows a generally increasing trend. In the Lorentzian fit we see a sharp increase in average shish length at low DR_d, and then an incremental growth at higher DR_d. This behavior is most significant in the Wi 0.64 ASF. Overall regardless of model, drawn structures from the lowest Wi ASF results in larger shish lengths, ranging between 550nm and 650nm. The higher Wi ASFs show very similar development of shish lengths. However, it is not clear whether this marks a significant difference and whether this difference leads to unique mechanical properties. We leave the mechanical testing as a function of DR_d for future studies.

4 Conclusions

Spinning: We conclude that the crystallization kinetics and final ASF crystalline structure uniquely depend on the magnitude of the maximum extension rate during spinning. We have quantified the effect of FIC on both the crystallization rate and the ASF
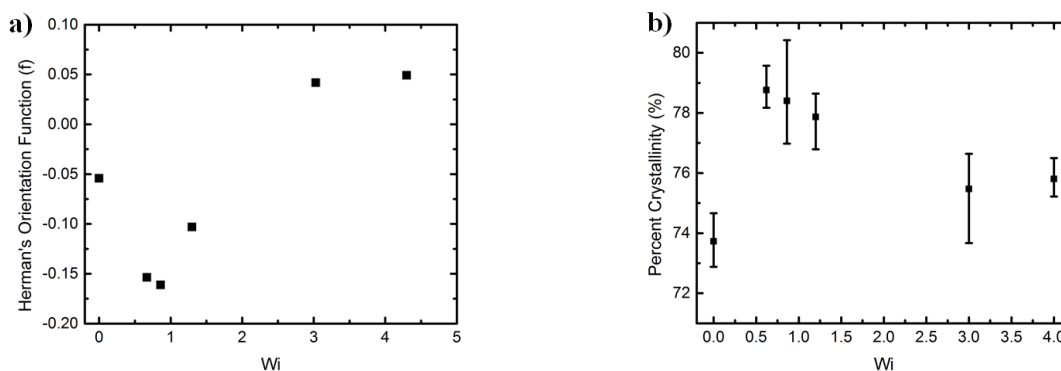
Fig. 10 (a) Hermans' Orientation function for the 2D SAXS patterns presented in Figure 9 as a function of the gel spinning Wiessenberg number, (b) Percent crystallinity as a function of Wi, as determined from WAXS.

crystalline structure. More specifically, increasing Wi strongly increases the crystallization kinetics and shifts the structure from isotropic lamellae to the onset of straight chain crystals. Regardless of experimental setup the crystallization time, measured during gel spinning, collapses onto a master curve when plotted against Wi. This suggests a monotonic dependence of crystallization rate on chain orientation and stretch. There is a clear asymptotic limit in crystallization time at increasing Wi, which we attribute to a molecular kinetic limitation previously alluded to through MD simulations. Asymptotic limits in both crystalline structure and percent crystallinity appear to correlate with crystallization kinetics; suggesting that the chain morphology during crystallization is not changing considerably with higher Wi. We show that the VR does not capture any physics of the gel spinning process and should be avoided at all cost. However, we realize that the characterization of Wi is nontrivial for industrial processes. In such situations, we suggest the use of the Capillary number to facilitate process-performance correlations.

Drawing: We show a direct correlation between initial ASF crystalline structure and PDF crystalline structure as a function of draw ratio. One similarity between all PDF structures is the development of straight chain crystal morphology at low post drawing DRs. In other words, straight chain crystals form very quickly during the post drawing process for the conditions studied here. The intensity and scattering pattern of lamellae domains are strongly dependent on the starting ASF crystalline structure. Quantitatively, low Wi ASFs have longer straight chain crystal domains than high Wi ASFs. The effect of crystalline morphology on "drawability" and mechanical properties is the subject of future investigations.

5 Acknowledgements

List of Abbreviations

ASF	as-spun fiber
Ca	Capillary number
DR_D	draw ratio calculated using measured diameters
DR_L	draw ratio calculated using change in length
DSC	differential scanning calorimetry
FIC	flow-induced crystallization
GPC	gel permeation chromatography
PDF	post drawn fiber
PE	polyethylene
SAOS	small amplitude oscillitory shear
SAXS	small-angle x-ray scattering
SEM	scanning electron microscopy
TEM	transmission electron microscopy
TGA	thermal gravimetric analysis
UHMWPE	ultra high molecular weight polyethylene
VR	ratio of wind-up to nozzle velocity
WAXS	wide-angle x-ray scattering
Wi	Weissenberg number

References

1 R. Marissen, *Materials Sciences and Applications*, 2011, **02**, 319–330.

2 B. Kalb and A. J. Pennings, *Polymer Bulletin*, 1979, **1**, 871–876.

3 P. Smith, P. J. Lemstra, B. Kalb and A. J. Pennings, *Polymer Bulletin*, 1979, **1**, 733–736.

4 A. J. Pennings and A. Zwijnenburg, *J. Polym. Sci.: Polym. Phys. Edit.*, 1979, **17**, 1011–1932.

5 J. Smook, M. Flinterman and A. J. Pennings, *Polymer Bulletin*, 1980, **2**, 775–783.

6 P. Smith, R. Koningsveld, C. J. H. Schoutetent and A. J. Pennings, *The British Polymer Journal*, 1980, 215–221.

7 P. Smith and P. J. Lemstra, *Journal of Polymer Science: Part B*, 1981, **19**, 1007–1009.

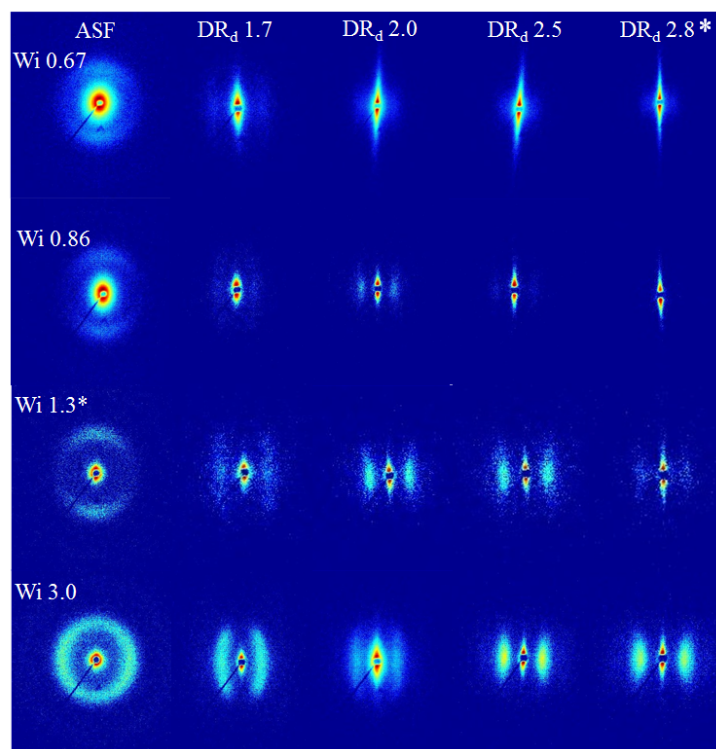8 J. Smook, W. Hamersma and A. J. Pennings, *Journal of Materials Science*, 1984, **19**, 1359–1373.

Fig. 11 2D SAXS patterns showing the development of crystalline structure for different starting ASF morphologies. Left to Right shows increasing DR_d as indicated at the top of the Figure. Top to Bottom shows increasing Wi number applied during Gel Spinning. The Wi=1.3, DR_d=2.8, denoted with *, represents DR_d=3.0
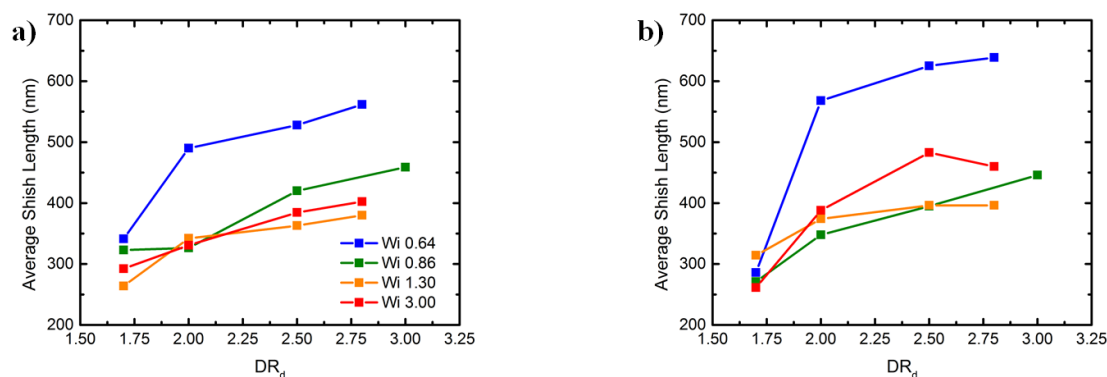

Fig. 12 Average shish length as a function of the applied draw ratio by fitting a: (a) Gaussian function.(b) Lorentzian function.

9 P. J. Barham and A. Keller, *Journal of Materials Science*, 1985, **20**, 2281–2302.

10 J. A. H. M. Moonen, W. A. C. Roovers, R. J. Meier and B. J. Kip, *Journal of Polymer Science Part B: Polymer Physics*, 1992, **30**, 361–372.

11 P. Smith, P. J. Lemstra and J. P. L. Pijpers, *Journal of Polymer Science, Part B: Polymer Physics*, 1982, **20**, 2229–2241.

12 C. W. M. Bastiaansen, *Polymer*, 1992, **33**, 1649–1652.

13 W. G. Perkins, N. J. Capiati and R. S. Porter, *Polymer Engineering and Science*, 1976, **16**, 200–203.

14 Y. Ohta, H. Murase and T. Hashimoto, *Journal of Polymer Science, Part B: Polymer Physics*, 2005, **43**, 2639–2652.

15 T. Jian, W.-d. Shyu, Y. Lin, K. Chen and J. T. Yeh, *Polymer Engineering & Science*, 2003, **43**, 1765–1777.

16 W. Hoogsteen, H. Kormelink, G. Eshuis, G. ten Brinke and A. J. Pennings, *Journal of Materials Science*, 1988, **23**, 3467–3474.

17 W. Hoogsteen, A. J. Pennings and G. ten Brinke, *Colloid & Polymer Science*, 1990, **268**, 245–255.

18 K. J. Smith and J. Wang, *Polymer*, 1999, **40**, 7251–7260.

19 A. J. Pennings and A. M. Kiel, *Kolloid-Zeitschrift & Zeitschrift fur Polymere*, 1965, **205**, 160–162.

20 A. J. Pennings, *Journal of Polymer Science Part C: Polymer Symposia*, 1967, **16**, 1799–1812.

21 T. Kanamoto, A. Tsuruta, K. Tanaka, M. Takeda and R. S. Porter, *Macromolecules*, 1988, **21**, 470–477.

22 M. Nakae, H. Uehara, T. Kanamoto, A. E. Zachariades and

List of Symbols

B_{obs}	azimuthal integral width
B_ϕ	Ruland streak misorientation parameter
D_0	initial fiber diameter/nozzle diameter
$D(p)$	diameter as function of position
$D(t)$	diameter as function of time
f	Hermans' orientation factor
G'	elastic moduli
G"	viscous moduli
h	convective heat transfer coefficient
I	scattering intensity
J_{evap}	evaporative flux
k	crystallization rate constant
L_c	characteristic length scale
$\langle L_{\text{shish}}\rangle$	average shish length
n	Avrami index
Q	volumetric flowrate
q	scattering vector
s	scattering parameter
T_c	isotropic crystallization temperature
T_{draw}	temperature during post drawing
T_g	glass transition temperature
T_{hopper}	hopper temperature
T_m	melt temperature
t_{81}	time required for fibers to reach 81°C
$t_{1/2}$	half crystallization time
V_c	crystalline volume fraction
V_{draw}	velocity during post drawing
V_{nozzle}	velocity of gel at the nozzle
V_{piston}	piston velocity
$V_{wind-up}$	velocity of the wind-up motor
Z	number of entanglements per chain
α	thermal diffusivity
$\dot\gamma$	characteristic strain rate
$\varepsilon_d(t)$	Hencky strain as function of time
$\varepsilon_{max,d}$	maximum strain at crystallization point
$\dot\varepsilon_d$	strain-rate applied during spinning
$\dot\varepsilon_{davg}$	average strain-rate applied during spinning
$\dot\varepsilon_{dmax}$	maximum strain-rate applied during spinning
λ	wavelength of x-rays
μ	dynamic viscosity
σ	surface tension
τ_c	relaxation time of one entanglement
τ_d	characteristic disengagement time
τ_k	crystallization time measured during spinning
τ_p	characteristic polymer relaxation time
τ_R	Rouse time
ω_d	crossover frequency

R. S. Porter, *Macromolecules*, 2000, **33**, 2632–2641.

23 D. M. Bigg, *Polymer Engineering and Science*, 1988, **28**, 830–855.

24 P. J. Barham, *Physics in Technology*, 1986, **17**, 167–173.

25 S. W. Mowry and G. C. Rutledge, *Macromolecules*, 2002, **35**, 4539–4549.

26 K. Anandakumaran, S. K. Roy and R. S. J. Manley, *Macromolecules*, 1988, **21**, 1746–1751.

27 W. Hoogsteen, G. ten Brinke and A. J. Pennings, *Polymer*, 1987, **28**, 923–928.

28 Y. Ohta, H. Murase and T. Hashimoto, *Journal of Polymer Science Part B: Polymer physics*, 2010, **48**, 1861–1872.

29 P. G. De Gennes, *The Journal of Chemical Physics*, 1974, **60**, 5030–5042.

30 T. T. Perkins, D. E. Smith and S. Chu, *Science*, 1997, **276**, 2016–2021.

31 A. T. Lorenzo, M. L. Arnal, J. Albuerne and A. J. Müller, *Polymer Testing*, 2007, **26**, 222–231.

32 C. W. Macosko, *RHEOLOGY Principles, Measurements, and Applications*, Wiley, 1984.

33 C. van der Walt, M. A. Hulsen, A. C. B. Bogaerds, H. E. H. Meijer and M. J. H. Bulters, *Journal of Non-Newtonian Fluid Mechanics*, 2012, **175-176**, 25–37.

34 J. Haudin, C. Duplay, B. Monasse and J. Costa, *Macromolecular Symposia*, 2002, **133**, 119–133.

35 R. M. Patel and J. E. Spruiell, *Polymer Engineering and Science*, 1991, **31**, 730–738.

36 B. Monasse, *Journal of Materials Science*, 1995, **30**, 5002–5012.

37 M. S. Lavine, N. Waheed and G. C. Rutledge, *Polymer*, 2003, **44**, 1771–1779.

38 G. Kumaraswamy, A. M. Issaian and J. A. Kornfield, *Macromolecules*, 1999, **32**, 7537–7547.

39 G. Kumaraswamy, R. K. Verma, A. M. Issaian, P. Wang, J. A. Kornfield, F. Yeh, B. S. Hsiao and R. H. Olley, *Polymer*, 2000, **41**, 8931–8940.

40 G. Kumaraswamy, J. A. Kornfield, F. Yeh and B. S. Hsiao, *Macromolecules*, 2002, **35**, 1762–1769.

41 B. Shen, Y. Liang, J. A. Kornfield and C. C. Han, *Macromolecules*, 2013, **46**, 1528–1542.

42 C. J. Geankoplis, *Transport processes and separation process principles: (includes unit operations)*, Prentice Hall Professional Technical Reference, 2003.

43 H. Murase, Y. Ohta and T. Hashimoto, *Polymer*, 2009, **50**, 4727–4736.

44 L. Fetters, D. J. Lohse and R. Colby, in *Physical Properties of Polymers Handbook*, ed. J. E. Mark, Springer, New York, NY, 2007, ch. 25, pp. 447–454.

45 Q. Huang, N. J. Alvarez, Y. Matsumiya, H. K. Rasmussen, H. Watanabe and O. Hassager, *ACS Macro Letters*, 2013, **2**, 741–744.

46 R. B. Bird, R. C. Armstrong and O. Hassager, *Dynamics of polymeric liquids*, Wiley, 1987.

47 J. K. Nielsen, H. K. Rasmussen, M. Denberg, K. Almdal and O. Hassager, *Macromolecules*, 2006, **39**, 8844–8853.

48 D. A. Nicholson and G. C. Rutledge, *Journal of Chemical Physics*, 2016, **145**, year.

49 W. J. Milliken and L. G. Leal, *Journal of Non-Newtonian Fluid Mechanics*, 1991, **40**, 355–379.

50 G. L. Leal, *Advanced Transport Phenomena: Fluid Mechanics and Convective Transport Processes*, Cambridge University Press, 2007.

51 S. L. Anna and H. C. Mayer, *Physics of Fluids*, 2006, **18**, year.

52 S. Lee and G. C. Rutledge, *Macromolecules*, 2011, **44**, 3096–3108.

53 J. T. Yeh, S. C. Lin, C. W. Tu, K. H. Hsie and F. C. Chang, *Journal of Materials Science*, 2008, **43**, 4892–4900.

54 P. B. McDaniel, J. M. Deitzel and J. W. Gillespie, *Polymer*, 2015, **69**, 148–158.

55 C. Fagnano, M. Rossi, R. S. Porter and S. Ottani, *Polymer*, 2001, **42**, 5871–5883.

56 W. Ruland, *Journal of Polymer Science Part C: Polymer Symposia*, 1969, **28**, 143–151.

57 R. Perret and W. Ruland, *J. Appl. Cryst.*, 1969, **2**, 209–218.

58 R. Perret and W. Ruland, *J. Appl. Cryst.*, 1970, **3**, 525–532.

59 J. K. Keum, F. Zuo and B. S. Hsiao, *Macromolecules*, 2008, **41**, 4766–4776.